PCCP

Accepted Manuscript

ROYAL SOCIETY OF CHEMISTRY

www.rsc.org/pccp

Physical Chemistry Chemical Physics

Cite this: DOI: 10.1039/c0xx00000x

www.rsc.org/xxxxxx

ARTICLE TYPE

Nanocomposite of Polyaniline and Nitrogen-doped Layered $HTiNbO_5$ with an Excellent Visible-light Photocatalytic Performance

Chao Liu[a], Liang Wu[a], Jing Chen*[b], Ji-yuan Liang[a], Chang-shun Li[a], Hong-mei Ji[a], Wen-hua Hou*[a]

Received (in XXX, XXX) Xth XXXXXXXXX 20XX, Accepted Xth XXXXXXXXX 20XX

DOI: 10.1039/b000000x

An effective approach has been used to synthesize N-doped $HTiNbO_5$ (denoted as N-$HTiNbO_5$) with a better intercalation property. The synthesis of polyaniline (PANI) with N-$HTiNbO_5$ to form PANI/N-$HTiNbO_5$ lamellar nanocomposite by *in situ* polymerization using aniline (ANI) intercalation compound ANI/N-$HTiNbO_5$ as the intermediate has been investigated. The resulted PANI/N-$HTiNbO_5$ nanocomposite showed a better crystallinity with a monolayer of PANI within the interlayers of N-$HTiNbO_5$, because nitrogen doping can affect the surface charge distribution of $[TiNbO_5]^-$ layers. The cyclic voltammetry (CV) results indicated that PANI/N-$HTiNbO_5$ nanocomposite had a good redox activity and electrochemical-cycling stability in acidic solution. The visible-light response of PANI/N-$HTiNbO_5$ nanocomposite was enhanced through N-doping, acid exchange, and the intercalation of PANI. PANI/N-$HTiNbO_5$ nanocomposite showed the highest activity with 97.8% methylene blue (MB) photodegraded in 170 min under visible light irradiation. The significant enhancement of photocatalytic performance can be attributed to the high efficiency of charge separation, induced by the synergistic effect between PANI and N-$HTiNbO_5$. In addition, PANI/N-$HTiNbO_5$ nanocomposite had a high thermal and photodegradation stability due to the intercalation reaction at a molecular level.

Introduction

Layered inorganic solids have been extensively investigated with the purpose of producing advanced materials through the intercalation of different guest species into the two-dimensional host interlayer region.[1-4] The resulting hybrid materials are receiving increasing attention because the synergism between host and guest often gives rise to properties that are superior to the sum of those of the individual components.

$KTiNbO_5$ is a typical layered white solid in which the alkali ions lie between layers built up form zigzag chains of edge-sharing MO_6 octahedra.[5] Recently, the protonated form, $HTiNbO_5$, has been studied as photocatalyst in view of its unique properties such as the layered structure, protonic acidity, and favorable charge transfer character.[5-7] However, like TiO_2, layered $HTiNbO_5$ itself has a relatively wide bandgap, showing some drawbacks such as its poor response to visible light, and high rate of electron-hole recombination.[7, 8]

In the past few years, some nonmetallic elements have been employed to tune the electronic structure of metal oxide semiconductors, in order to enhance the photocatalytic activity under visible light irradiation.[9, 10] Recently, it was found that TiO_2 doping with nonmetallic elements such as N, S, B and C exhibited red-shifted absorption spectra, lowered oxidation potentials, and the decreased band gap energy.[10-12] In our group, in order to enhance the visible-light photocatalytic activity, $HTiNbO_5$ was first exfoliated and then calcinated with urea to realize N-doping, but its intercalation property was greatly destroyed.[7] Accordingly, we attempt to develop another effective approach to synthesize N-doped $HTiNbO_5$ with its intercalation property maintained.

PANI has been intensively studied due to its advantages of low cost, electron and hole transporting properties, high conductivity, ease of synthesis and good environmental stability.[13] Furthermore, PANI in its undoped or partially doped states is an electron donor upon photoexcitation, and is known as a good hole conductor.[14] Conducting PANI behaves as a p-type semiconductor with a narrow band gap, and it has a band-gap absorption edge that can extend into the range of visible light.[15] Thus, p-n junctions can be realized by intercalating a p-type PANI into the n-type layered N-$HTiNbO_5$. This should allow the drawbacks of the latter, such as its poor response to visible light, high rate of electron-hole recombination, to be overcome.

Composites containing PANI and other semiconductor photocatalysts have been synthesized and demonstrated higher photocatalytic activity of pollutant degradation. A magnetically recyclable $CoFe_2O_4$/PANI photocatalyst has been prepared with a high photocatalytic activity for the degradation of dyes under UV and visible light irradiation.[16] The Cu_2O/PANI nanocomposites have been successfully synthesized *via* a simple, one-step hydrothermal method and showed a high photocatalytic activity

for the degradation of dyes under visible light irradiation than TiO_2 and pure Cu_2O.[17] Ge et al. have prepared *g*-C_3N_4/PANI composite which exhibited the enhanced photocatalytic activities in the degradation of MB dye.[18] Furthermore, the composite photocatalysts, such as ZnO/PANI,[19] CuI/PANI,[20] TaON/PANI,[21] and Bi_3NbO_7/PANI,[22] have also been developed and demonstrated efficient photocatalytic activity. However, in these composites, PANI was loaded only on the surface of Cu_2O, ZnO, CuI, TaON and Bi_3NbO_7, which inevitably caused a lower thermal stability and photodegradation stability than these PANI-intercalated layered composites.

Through an electrophoretic deposition (EPD) method, PANI intercalated layered protonic titanate (LPT) was synthesized and exhibited a much higher photocatalytic activity for the degradation of MB in aqueous solution under visible light irradiation than semiconducting LPT itself.[15] However, only a small amount of PANI/LPT composite could be prepared each time, which limited its practical application. Thus, it was necessary to prepare PANI/N-$HTiNbO_5$ nanocomposite *via* intercalation reaction. This should allow the above drawbacks, such as low thermal stability, low photodegradation stability and low yield, to be overcome. Additionally, to our knowledge, there is no report on the synthesis and photoactivity in the PANI/N-$HTiNbO_5$ system.

In this work, PANI/N-$HTiNbO_5$ layered nanocomposite was first prepared by *in situ* polymerization of aniline in the confined interlamellar galleries of N-doped layered $HTiNbO_5$. The structure, surface morphology, thermal stability, electrochemical properties and visible-light photocatalytic performance in the degradation of MB of the resulted PANI/N-$HTiNbO_5$ have been studied and discussed in detail. Moreover, a possible photocatalytic mechanism was proposed based on the experimental results.

Experimental Section

Synthesis of N-doped $HTiNbO_5$ and the corresponding aniline- and polyaniline- intercalated composites

The layered compound $KTiNbO_5$ was synthesized by heating a stoichiometric mixture of K_2CO_3, TiO_2 and Nb_2O_5 in molar ratios of 1:2:1 at 1100 °C for 24 h, according to the procedure described in the literature.[23] The protonated form $HTiNbO_5$ was obtained by the treatment of $KTiNbO_5$ with 5 M HNO_3 aqueous solution at room temperature for 3 days. During the proton exchange reaction, the acid solution was replaced with a fresh one every 24 h.

To prepare N-doped $KTiNbO_5$ materials (denoted as N-$KTiNbO_5$), $KTiNbO_5$ (2.00 g) was finely milled with urea (4.00 g), and then the resulting mixture was heated in air at 400 °C for 5 h. The protonated form N-$HTiNbO_5$ was obtained by the treatment of N-$KTiNbO_5$ with 5 M HNO_3 aqueous solution at room temperature for 3 days. During the proton exchange reaction, the acid solution was replaced with a fresh one every 24 h.

To prepare aniline-intercalated N-doped $HTiNbO_5$ (termed as ANI/N-$HTiNbO_5$), 1.50 g N-$HTiNbO_5$ was dispersed in 60 mL distilled water, and then 3 mL aniline that had been distilled in vacuum was added. The acid/base reaction of aniline with protons of the layered host was the main driving force of the intercalation. The mixture was stirred for 2 days at room temperature. The monomer-intercalated product was filtered, washed thoroughly with distilled water and absolute ethanol several times until the UV absorption of the washed solutions did not present any peaks of aniline, and finally dried at room temperature in vacuum.

The polymerization of intercalated aniline monomers was realized by treatment of ANI/N-$HTiNbO_5$ with $(NH_4)_2S_2O_8$ in an ice bath for 24 h. 1 g ANI/N-$HTiNbO_5$ was added to an aqueous solution of 10 mL $(NH_4)_2S_2O_8$ (1 M) and HCl (0.1 M), and then stirred in an ice bath for 24 h. The final nanocomposite PANI/N-$HTiNbO_5$ was centrifuged and washed with distilled water and ethanol several times, and dried at 50 °C in vacuum overnight. For comparison, PANI/$HTiNbO_5$ nanocomposite was also prepared through a similar process in which only N-doped $HTiNbO_5$ was replaced by $HTiNbO_5$.

Characterization

Thermogravimetric and differential scanning calorimetric analyses (TG-DSC) were performed with a Shimadzu TGA-50 under an air flow, and the measurements were conducted from room temperature to 1000 °C at a heating rate of 10°C min^{-1}. The X-ray diffraction (XRD) patterns of the obtained samples were taken on a Philip-X'Pert X-ray diffractometer with a Cu Kα radiation (λ = 1.5418 Å) and Ni filter at a scanning rate of 0.2°/s in a 2θ range of 5~60°. UV-vis diffuse reflectance spectra were obtained on a UV-vis spectrophotometer (Shimadzu, UV-2401) using $BaSO_4$ as reference. Fourier transformed infrared (FTIR) spectra were recorded using KBr pellets on a Bruker Vector 22 FTIR spectrometer (Billerica, MA). The morphology was investigated by scanning electron microscopy (SEM, JEOL JEM-6300F) and transmission electron microscopy (TEM, JEOL JEM-200CX, operating at an accelerating voltage of 200 kV). For TEM observation, the samples were dispersed in ethanol by ultrasonic treatment and dropped onto carbon-coated copper grids. Photoluminescence (PL) spectra were recorded on a 48000DSCF luminescence spectrometer at room temperature by using a continuous-wave 325 nm He-Cd laser as the excitation source. The samples were pressed into a thin disk and fixed in a homemade quartz cell.

Cyclic Voltammetry

Electrochemical measurements were performed with a conventional three-electrode electrochemical cell at room temperature, using a platinum wire as the counter electrode and a saturated calomel electrode (SCE) as the reference electrode. The glassy carbon electrode (GCE, area 0.38 cm^2) was hand polished directly with slurry of 1.0 and then 0.3 μm alumina. The obtained nanocomposite was dispersed in distilled water, drop-coated onto the surface of GCE as the working electrode. Cyclic voltammetry (CV) scans were carried out in aqueous HCl solution on a CHI660D Electrochemical Workstation at different scan rates of 10 to 500 mV s^{-1} between –0.4 and +0.8 V. Prior to the measurement, the working electrode coated with nanocomposite was immersed in electrolyte solution for 30 min to assure the diffusion of solution into the interlayers and thus permit a better ionic exchange.

Adsorption Experiments

For adsorption experiments, different materials were added

into the flask containing 100 mL of MB solution with an initial concentration of 30 mg/L under magnetic stirring for 45 min in the dark. Samples were collected at different time intervals (0, 5, 10, 15, 20, 25, 30, 35, 40 and 45 min, respectively), and the dye concentration was determined by a Shimadzu UVmini-1240 UV-vis spectrophotometer. The dye concentrations were calibrated using the Beer–Lambert law at λ_{max} values of 663.5 nm for MB. After adsorption of the dye, the materials were washed with distilled water, and redispersed in 100 mL of MB solution for photocatalytic reaction.

Visible-light Photocatalytic Reaction Tests

The visible light photocatalytic activity was evaluated by the degradation of MB in aqueous solution after the adsorption of MB reached its equilibrium. 30 mg of catalyst was suspended in an aqueous solution (100 mL) of MB (1×10^{-5} M) in a beaker. The suspension was stirred for 45 min to establish an adsorption/desorption equilibrium before irradiation in a reaction cell. Light from a 300 W Xe lamp passed through a UV light filter film (to remove radiation with $\lambda < 420$ nm) and was focused onto the reaction cell. The optical power and power density were recorded on a CEL-NP2000 (see Table S1). When the light was turned on, at given time intervals, approximately 4 mL of the reaction suspension was sampled and separated by means of high-speed centrifugation. The filtrates were analyzed by recording the maximum absorbance at 663.5 nm in the UV-visible spectrum of MB. The degradation efficiency at time t was determined from the value of C_t/C_0, where C_0 is the initial concentration and C_t is the concentration of MB at the irradiation time t.

Results and Discussion

Thermogravimetric analysis of nanocomposites

Fig. 1 presents TG-DSC curves of $HTiNbO_5$, N-$HTiNbO_5$, bulk PANI, PANI/N-$HTiNbO_5$, and PANI/$HTiNbO_5$. For $HTiNbO_5$ (Fig. 1a), the weight loss (ca. 4.9 wt%) originates from the dehydration of water in the interlayer spacing and the collapse of $TiNbO_5^{-1}$ layers to produce new phase after complete dehydration.[15] Compared with $HTiNbO_5$, N-$HTiNbO_5$ (Fig. 1b) showed a relatively higher exothermic peak (852 *vs* 735 °C). It indicates that N-$HTiNbO_5$ has a higher thermal stability than $HTiNbO_5$. For pure PANI (Fig. 1c), the weight loss at a temperature lower than 129 °C is mainly due to the loss of adsorbed water molecules. The PANI is stable between 129 and 223 °C, whereas degradation occurs at a higher temperature, showing a similar behavior with other studies.[15, 24] The weight loss starting at ~300 °C is assigned to the thermal decomposition of PANI backbone chains.[25, 26] The TG-DSC curve of PANI/N-$HTiNbO_5$ (Fig. 1d) exhibits a three-step weight loss process. The first weight loss below 150 °C is attributed to the release of free water (ca. 3 wt%). The second weight loss (ca. 4.6 wt%) ranging from 150 to ~431 °C is due to the dehydration of $HTiNbO_5$ and the elimination of dopant (HCl) from the polymer structure.[27, 28] The third weight loss (ca. 6.9 wt%) above 431 °C is assigned to the thermal decomposition of intercalated PANI. In the case of PANI/N-$HTiNbO_5$ nanocomposite, the exothermic peak ascribed to the decomposition of intercalated PANI appears at 518°C, while that for the decomposition of pure PANI being at 398°C. In

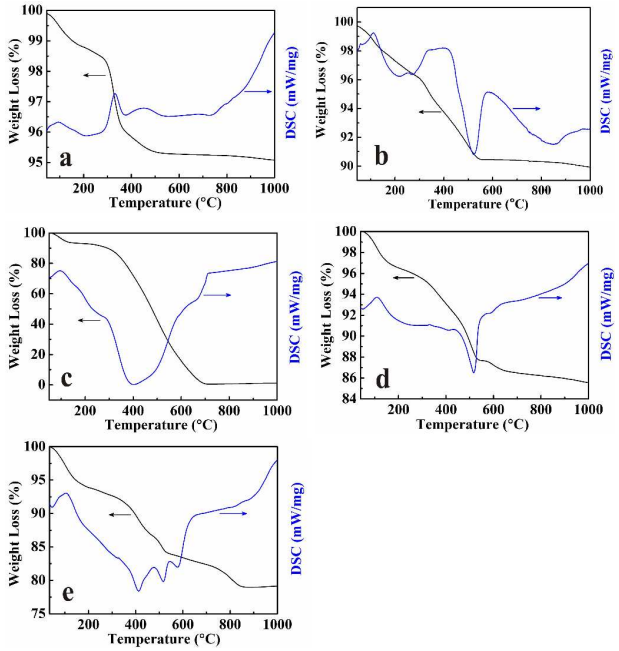

Fig. 1 TG-DSC curves of (a) $HTiNbO_5$, (b) N-$HTiNbO_5$, (c) bulk PANI, (d) PANI/N-$HTiNbO_5$, and (e) PANI/$HTiNbO_5$.

addition, the pure PANI synthesized by chemical polymerization shows degradation in a much wider temperature range. These results suggest that the intercalated system is more thermally stable, and PANI within N-$HTiNbO_5$ layers have a much narrower molecular weight distribution than bulk PANI. By comparison, PANI/$HTiNbO_5$ (Fig. 1e) nanocomposite shows three exothermic peaks at 411, 518 and 579 °C, respectively, corresponding to the decomposition of intercalated PANI molecules with different molecular weights between layers. It indicates that PANI/N-$HTiNbO_5$ nanocomposite shows the higher thermal stability than PANI/$HTiNbO_5$ nanocomposite. The above results suggest that nitrogen doping can affect the surface charge distribution of $[TiNbO_5]^-$ layers, and PANI/N-$HTiNbO_5$ has a better crystallinity than PANI/$HTiNbO_5$.

Powder X-ray Diffraction (XRD) Analysis

The layered structure and crystallinity of the samples were identified by XRD. The XRD pattern of the as-prepared layered $KTiNbO_5$ (Fig. 2a) matches well with the published data (PDF, #54-1155).[1] After doping with nitrogen through heating $KTiNbO_5$ with urea at 400 °C for 5h, all the characteristic peaks of the layered structure were almost unchanged (Fig. 2b). The layered structure was well retained for N-doped $KTiNbO_5$ samples prepared at 300, 450 and 500°C, respectively. However, only the sample prepared at 400°C shows a yellow colour (Fig. S1). Since the interlayer distance of N-$KTiNbO_5$ is 9.20 Å, the thickness of N-doped $[TiNbO_5]^-$ layer is calculated to be 6.80 Å by subtracting the diameter (~2.4 Å) of the interlayered K^+ ions. As we know, the direct intercalation of bulky ions into interlayer spacing of N-$KTiNbO_5$ is difficult due to the high charge densities of N-doped $[TiNbO_5]^-$ layers. However, the protonated form N-$HTiNbO_5$ shows a relatively strong Brønsted acidity and is an ideal 2D host for the intercalation of basic monomers such as aniline.[1] It has an interlayer distance of 8.27 Å (Fig. 2c). Upon intercalation with aniline, the characteristic (002) reflection peak

is shifted toward a lower 2θ angle. As shown in Fig. 2d, the monomer composite ANI/N-HTiNbO$_5$ has an interlayer distance of 12.65 Å. By subtracting the thickness of N-doped $[TiNbO_5]^-$ slab, the interlayer spacing is estimated to be 5.85 Å which is 0.84 times the molecular length of ANI (ca. 7.0 Å). This means that the intercalated ANI molecules should be oriented in a monolayer arrangement within the layers.

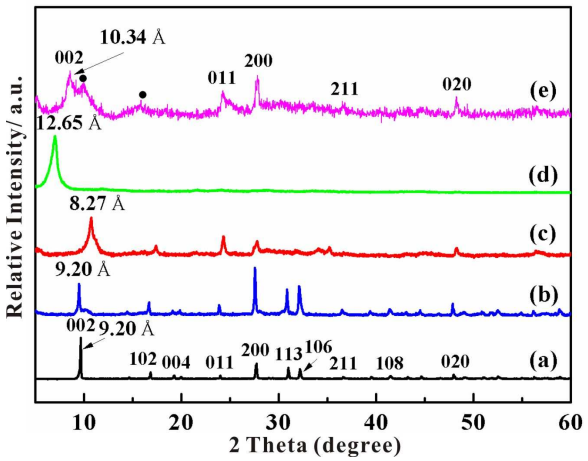

Fig. 2 X-ray power diffraction patterns of (a) KTiNbO$_5$, (b) N-KTiNbO$_5$, (c) N-HTiNbO$_5$, (d) ANI/N-HTiNbO$_5$, and (e) PANI/N-HTiNbO$_5$ (dark points denote the peaks of PANI).

Being initiated by oxidant $(NH_4)_2S_2O_8$, the interlayered aniline monomers were polymerized *in situ* to form PANI and thus the interlayer distance changed correspondingly (Fig. 2e). The XRD pattern of PANI/N-HTiNbO$_5$ shows a weak (002) characteristic peak at 8.53° (d_{002} = 10.34 Å) and some new peaks (denoted by dark points) attributed to the PANI on the edge of N-HTiNbO$_5$.[29] Due to the polymerization of aniline within the confined interlayers, PANI/N-HTiNbO$_5$ shows a lower degree of crystallinity. Nevertheless, the layered structure was still retained after polymerization. Judging from the layer distance of PANI/N-HTiNbO$_5$, the gallery height occupied by PANI molecules in the interlayers is estimated to be 3.54 Å, which is comparable to the size of benzene ring within PANI. This is suggestive of a monolayer packing of PANI molecules, and as a result, the benzene rings were more flattened against the layer surface of N-HTiNbO$_5$.

Morphology and Structure of Nanocomposites

As shown in Fig. 3a, the layered structure of the as-prepared KTiNbO$_5$ is clearly visible. The layered structure of KTiNbO$_5$ was still maintained after N-doping (Fig. 3b), but was relatively less ordered and the surface roughness of the lamellar plates was increased. Fig. S2 shows the EDS mapping of N-KTiNbO$_5$, confirming that nitrogen ions are homogeneously distributed in the compound. After exchange with H^+, the protonated form N-HTiNbO$_5$ shows a similar morphology, with a little disorder on the edge of particles due to the proton exchange (Fig. 3c). Interestingly, the resulting PANI/N-HTiNbO$_5$ nanocomposite retains significantly nanolayer structure but the surface and edges become out-of-flatness, despite the fact that the overall crystallinity was decreased (Fig. 3d). It is also possible to notice that the morphology of PANI/N-HTiNbO$_5$ nanocomposite is more similar to that of the layered host N-HTiNbO$_5$, when compared with the aggregated ball-like morphology of the pure PANI. This results suggests that the polymerization occurs mainly between inorganic layers, which is consistent with XRD patterns. Moreover, as the PANI chains extend from the interlayers and link with each other among the adjacent crystals, PANI/N-HTiNbO$_5$ crystal is aggregated and its size is larger than those of KTiNbO$_5$, N-KTiNbO$_5$, N-HTiNbO$_5$.[30]

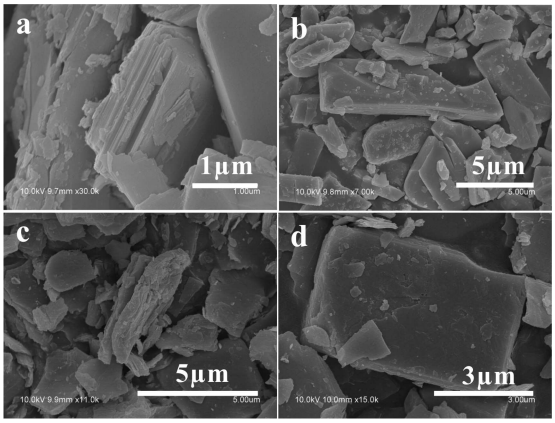

Fig.3 SEM micrographs of (a) KTiNbO$_5$, (b) N-KTiNbO$_5$, (c) N-HTiNbO$_5$, and (d) PANI/N-HTiNbO$_5$.

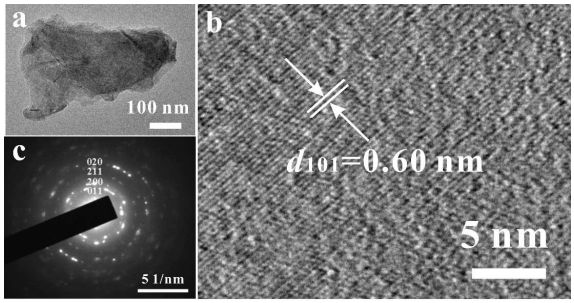

Fig. 4 TEM (a), HRTEM (b), and SAED pattern (c) of PANI/N-HTiNbO$_5$ nanocomposite.

As shown in TEM images, the surfaces of PANI/N-HTiNbO$_5$ nanocomposite show relatively homogeneous and overlapped sheets. The layered nature can be clearly observed in Fig. 4a. This is consistent with a typical topotactic intercalation in which the layer structure and morphology are preserved after intercalation and polymerization. A HRTEM image (Fig. 4b) reveals that the resulting PANI/N-HTiNbO$_5$ nanocomposite exhibits the lattice fringe with interplannar spacing of 0.60 nm, corresponding to the (101) plane. As shown in the corresponding selected area electron diffraction (SAED) pattern (Fig. 4c), diffraction spots with *d* values of 3.68, 3.21, 2.43 and 1.88 nm, corresponding to the (011), (200), (211) and (020) planes, respectively, which is consistent with XRD results above.

Fourier Transformed Infrared (FTIR) Spectroscopy

FTIR spectra of KTiNbO$_5$, N-KTiNbO$_5$, PANI/HTiNbO$_5$ and PANI/N-HTiNbO$_5$ nanocomposites are shown in Fig. 5. The characteristic bands of KTiNbO$_5$ were still maintained after N-doping (Fig. 5b). In the FTIR spectrum of PANI/N-HTiNbO$_5$ (Fig. 5d), a number of characteristic bands of PANI, such as1160 cm^{-1} (N=Q=N stretching, Q=N^+H−B stretching, B and Q as benzenoid and quinonoid units), 1242 cm^{-1} (aromatic C−H in-plane bending, C−N stretching in BBB), 1311 cm^{-1} (C−N

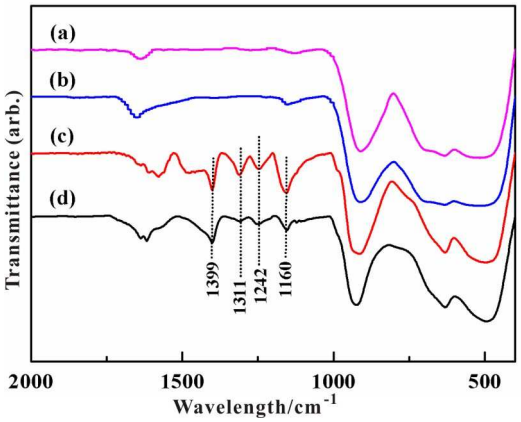

Fig. 5 FTIR spectra of (a) $KTiNbO_5$, (b) N-$KTiNbO_5$, (c) PANI/$HTiNbO_5$, and (d) PANI/N-$HTiNbO_5$.

stretching in QB_cQ, QBB, BBQ, c as *cis*.), and 1399 cm^{-1} (C–N stretching in QB_tB, t as *trans*.), can be observed.[31, 32] In addition, other absorption peaks which are attributed to the Nb–O and Ti–O stretching vibrations are also observed between 400 and 1000 cm^{-1}, confirming the hybridization of N-$HTiNbO_5$ with PANI.

UV-visible diffuse reflectance spectra

As shown in Fig. 6, a strong absorption band can be observed in the UV region for $KTiNbO_5$, N-$KTiNbO_5$, N-$HTiNbO_5$, and PANI/N-$HTiNbO_5$ nanocomposite, which is attributed to the band-to-band transition. After N-doping, N-$KTiNbO_5$ shows a significant absorption tail in the visible region between 400 and 600 nm. Fig. S3 shows UV-visible diffuse reflectance spectra of N-doped $KTiNbO_5$ samples prepared at different temperatures, and the sample prepared at 400 °C has the lowest band gap of 3.15 eV. After exchange with H^+, the absorption edge of the resulted N-$HTiNbO_5$ has a red shift to some extent compared than N-$KTiNbO_5$, and N-$HTiNbO_5$ showed a stronger absorption than N-$KTiNbO_5$. PANI shows two peaks at 438.3 and 644.7 nm, which are attributed to the excitations of amine and imine groups, respectively.[33] The spectrum of the resultant PANI/N-$HTiNbO_5$ nanocomposite presents two absorptions. The former absorption with a maximum at 534.8 nm is assigned to π–π* transition of benzenoid rings and the latter band at 729.4 nm is assigned to electron transition from benzenoid to quinoid rings of the intercalated PANI,[34, 35] giving rise to the enhanced visible-light response compared with N-$HTiNbO_5$. The absorption peak at 644.7 nm for bulk PANI has shifted to 729.4 nm for PANI/N-$HTiNbO_5$ nanocomposite. This shifting of the peak to higher wavelength indicates an increase of conjugation length, a decrease of band gap energy, and a delocalization of electrons in the polaron band.[35, 36] This is attributed to the more extended chain conformation of PANI in PANI/N-$HTiNbO_5$ nanocomposite as compared with pure PANI, and the fact that the intercalated PANI molecules are doped by protons of N-$HTiNbO_5$, with $[NTiNbO_5]^-$ slabs acting as the counter anions.

Generally speaking, the intensity and position of the absorption peaks are mainly affected by two factors. The first is the extent of oxidization of the intercalated PANI molecules, which can be simply estimated by the intensity ratio of $I(\pi-\pi^*)/I(n-\pi^*)$,[1, 37] the second is the extent of doping of the intercalated PANI molecules by protons of N-$HTiNbO_5$, which is dependent on the shift value of the two absorptions. In PANI/N-$HTiNbO_5$ nanocomposite, the adsorption of a quinoid ring is shifted to 729.4 nm and the intensity ratio of $I(\pi-\pi^*)/I(n-\pi^*)$ is higher than that of pure PANI. Two conclusions can be reached from these results. First, the oxidization extent of the intercalated PANI molecules is somewhat lower than that of bulk PANI because the confined interlayer space limits the migration of the oxidant. Second, the proton-doping extent of PANI/N-$HTiNbO_5$ is lower than that of bulk PANI salt (doped by HCl) and the interlayered protons are partially doped at the –N= of the quinoid rings. The above results suggest that N-doping and PANI intercalation can enhance the absorption in the visible-light region.

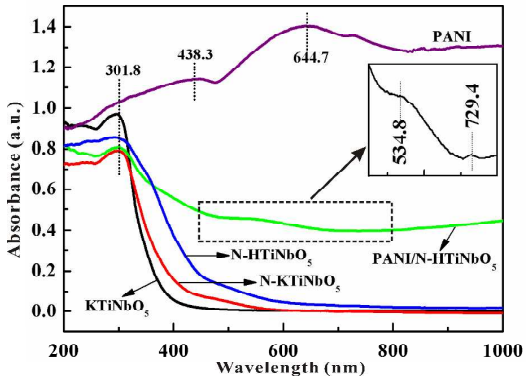

Fig. 6 Diffuse reflection UV-visible spectra of PANI, $KTiNbO_5$, N-$KTiNbO_5$, N-$HTiNbO_5$, and PANI/N-$HTiNbO_5$ nanocomposite (Inset shows the magnified spectrum of PANI/N-$HTiNbO_5$).

Cyclic Voltammetry and Electroactivity of Nanocomposite

Electrochemical experiments on PANI/N-$HTiNbO_5$ nanocomposite were carried out by using CV. As show in Fig. 7a, there are two reduction peaks observed at 0 and 0.28 V for PANI/N-$HTiNbO_5$ nanocomposite in HCl solution with a higher concentration. As the concentration of HCl solution is decreased gradually, the reduction peaks merge to show only one broad at 0.1 V. This redox behavior is similar to that reported previously.[38, 39] The redox peaks of PANI/N-$HTiNbO_5$ nanocomposite can be discussed based on the known models of bulk PANI. As we know, PANI exists three well-defined oxidation states: leucoemeraldine, emeraldine and pernigraniline. In the leucoemeraldine state, all the nitrogen atoms are amines, whereas in pernigraniline, the nitrogen atoms are imines. The emeraldine state consists of alternating reduced and oxidized groups. The emeraldine can be converted between its base and salt forms, depending on the pH value. The first reduction peak around 0 V is due to the redox transition of PANI between leucoemeraldine state and emeraldine salt state, and the second one at around 0.28 V can be assigned to the emeraldine salt and pernigraniline state transformation. The reduction peak around 0.1 V in lower concentration HCl solution is ascribed to the overlapping of two redox processes of PANI normally found in acid conditions, that is, transition between fully reduced leucoemeraldine base (LEB) form and half-oxidized EB form, and that between EB form and fully oxidized pernigraniline base (PNB) form.

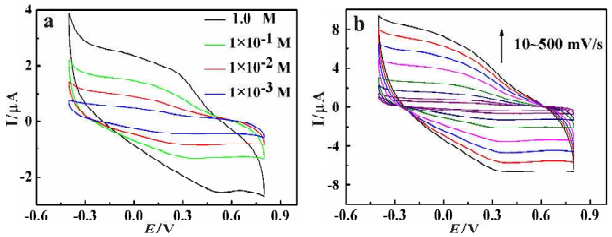

Fig. 7 Cyclic voltammograms of PANI/N-HTiNbO$_5$ thin film (a) with different HCl concentrations, and (b) in 0.1 M HCl solution at different scan rates (10, 20, 50, 100, 200, 300, 400, 500 mV s^{-1}).

The CVs of PANI/N-HTiNbO$_5$ nanocomposite measured in 0.1 M HCl solution reveal that the peak current is increased with the scan rate (Fig. 7b), indicating a good ability of ions insertion/deinsertion between the layers. The redox behavior of nanocomposite may originate from the fact that the layered host provides a two-dimensional channel for the conducting carriers.

Fig. S4 shows the CV curve of PANI/N-HTiNbO$_5$ nanocomposite upon repeated potential cycling for 50 cycles in the potential range between –0.4 and +0.8V. It can be seen that PANI/N-HTiNbO$_5$ nanocomposite is very stable in acid condition, and the peak current and peak-to-peak separation of the 50th cycle is almost the same with those of the first cycle. Thus, the excellent electrochemical stability and reproducibility offer interesting opportunities for practical application.

Study of MB Adsorption and Visible Light Photocatalytic Activities Performance

Fig. 8a shows the adsorption of MB with time in the presence of PANI, KTiNbO$_5$, HTiNbO$_5$, N-KTiNbO$_5$, N-HTiNbO$_5$, PANI/HTiNbO$_5$ and PANI/N-HTiNbO$_5$, respectively. It is obvious that there is no significant adsorption of cationic dye MB onto PANI, KTiNbO$_5$, HTiNbO$_5$, N-KTiNbO$_5$ and N-HTiNbO$_5$. However, for PANI/HTiNbO$_5$ and PANI/N-HTiNbO$_5$, a significant adsorption can be observed. Because the positively charged groups of the dye and positively charged backbone of PANI repel each other,[16] the enhanced adsorption ability of PANI/HTiNbO$_5$ and PANI/N-HTiNbO$_5$ composites are due to the extended PANI chains with a highly unordered conjugation and small amount PANI bridges to form the porous structure of these two nanocomposites.[1, 30]

Due to the significant adsorption capacity of photocatalysts, it is necessary that the photocatalytic systems were magnetically stirred for more than 45 min in the dark. The photocatalytic activities of composite samples were investigated by choosing the photodegradation of MB dye in aqueous solution under visible light ($\lambda > 420$ nm) at room temperature. The target molecule MB is relatively stable in aqueous solutions under visible light irradiation. Furthermore, a photodegradation reaction could not be observed in the presence of PANI/N-HTiNbO$_5$ nanocomposite when the reaction mixture was maintained in the dark. The characteristic absorption of MB at $\lambda = 663.5$ nm was employed to monitor the photocatalytic degradation process. Fig. 8b shows the photocatalytic activities of PANI, KTiNbO$_5$, HTiNbO$_5$, N-KTiNbO$_5$, N-HTiNbO$_5$, PANI/HTiNbO$_5$ and PANI/N-HTiNbO$_5$.

It has been reported that some dyes can absorb visible light and be excited.[16] The excited state can be degraded by self-sensitization when the energy level of the conduction band of itself matches that of photocatalyst. For instance, MB can absorb visible light with a wavelength longer than 600 nm (the absorption peak is at ~663.5 nm), and was excited during the photocatalytic process.[40] As shown in Fig. 8b, the degradation of MB was neglectable in the absence of photocatalyst under visible light irradiation. The pure PANI sample also showed almost no photodegradation. However, there was a non-negligible decrease of MB concentration in solution in the presence of KTiNbO$_5$ and HTiNbO$_5$, which is essentially due to the self-photosensitized oxidation. Compared with KTiNbO$_5$, N-KTiNbO$_5$ showed a relatively higher photodegradation percentage (79.0% *vs* 41.9%) of MB under visible light in 170 min, indicating the promoting effect of N-doping for visible light photocatalytic performance. After exchange with H$^+$, the resulted HTiNbO$_5$ and N-HTiNbO$_5$ shows an enhanced photocatalytic performance compared with KTiNbO$_5$ and N-KTiNbO$_5$, respectively, due to the increase of acidity.[41] Furthermore, a significantly enhanced photocatalytic performance was observed in PANI/HTiNbO$_5$ and

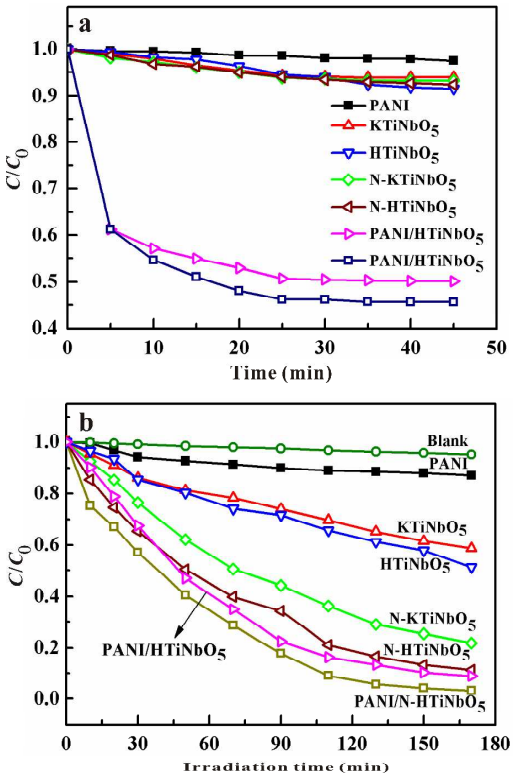

Fig. 8 (a) The adsorption capacity of MB with time, and (b) visible light photocatalytic degradation rate of MB over PANI, KTiNbO$_5$, HTiNbO$_5$, N-KTiNbO$_5$, N-HTiNbO$_5$, PANI/HTiNbO$_5$, and PANI/N-HTiNbO$_5$.

PANI/N-HTiNbO$_5$. PANI/N-HTiNbO$_5$ nanocomposite showed the highest activity with 97.8% MB photodegraded in 170 min. It indicates that the intercalation of PANI is effective for the enhanced photocatalytic performance. Therefore, the observed photobleaching in the photocatalytic process should be mainly due to the oxidative photodegradation of the dye molecules rather than adsorption.

As we know, the photocatalytic reaction depends largely upon the life of electron–hole pair. Photoluminescence (PL) emission spectra can be used to study the photogenerated charge carrier separation and to understand the role of PANI in enhancing visible light activity for MB degradation.[18] Fig. 9 shows the PL

spectra of $KTiNbO_5$, N-$KTiNbO_5$, PANI/$HTiNbO_5$, and PANI/N-$HTiNbO_5$ with an excitation wavelength of 325 nm. The main emission peak is centered at about 468 nm for various samples, which can be ascribed to the band gap recombination of electron–hole pairs.[42, 43] The PL of two nanocomposites was suppressed and showed a diminished PL intensity compared with bare $KTiNbO_5$ and N-$KTiNbO_5$. It indicates a reduced charge recombination and thus the intercalation of PANI is effective for electron–hole pair separation. On the other hand, it can be also observed that N-doped samples (N-$KTiNbO_5$ and PANI/N-$HTiNbO_5$) have an obviously reduced PL intensity compared with their undoped counterparts, indicating the beneficial effect of N-doping for electron–hole pair separation. These could be reasons why PANI/N-$HTiNbO_5$ demonstrated the highest activity for MB degradation.

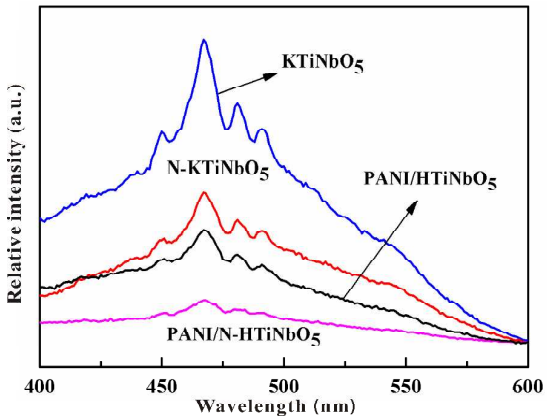

Fig. 9 PL spectra of $KTiNbO_5$, N-$KTiNbO_5$, PANI/$HTiNbO_5$ and PANI/N-$HTiNbO_5$ with an excitation wavelength of 325 nm.

The visible light photocatalytic activities of the obtained PANI/N-$HTiNbO_5$ sample were mainly studied by the photodegradation of MB aqueous solution (Fig. 10). UV–visible spectra of MB exhibited three bands at 240, 296, and 665 nm. In Fig. 10a, the rapid decrease in absorption intensity of all bands shows that MB is efficiency degraded under visible light irradiation in the presence of PANI/N-$HTiNbO_5$ nanocomposite. The results confirm that the visible light response of N-$HTiNbO_5$ has been significantly enhanced by the formation of PANI/N-$HTiNbO_5$ nanocomposite.

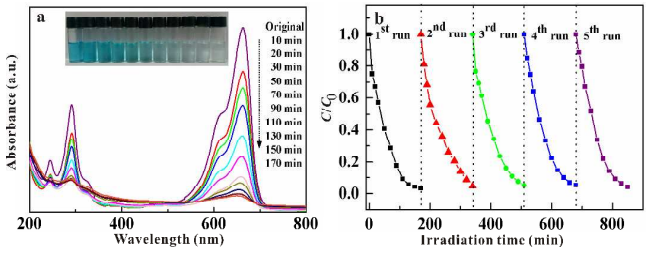

Fig. 10 (a) UV-visible spectral and color changes, and (b) photodegradation stability of MB over PANI/N-$HTiNbO_5$ under visible light irradiation.

Besides the enhanced photocatalytic activity resulting from N-doping and PANI intercalation, the photostability of the photocatalyst was also retained. The circulating runs in the photocatalytic degradation of MB in the presence of PANI/N-$HTiNbO_5$ under visible light were checked. After five recycles, the catalyst did not exhibit any significant loss of activity (Fig. 10b). It indicates that PANI/N-$HTiNbO_5$ has a high stability and does not photocorrode during the photocatalytic oxidation of the pollutant molecules.

Photocatalytic mechanism

Based on the above results, a possible mechanism for the photocatalytic degradation of MB over PANI/N-$HTiNbO_5$ catalyst was proposed and is schematically shown in Fig. 11. When PANI/N-$HTiNbO_5$ is illuminated under visible light irradiation, both N-$HTiNbO_5$ and PANI absorb photons and then charge separation occurs at the interface. The CB of N-$HTiNbO_5$ and the lowest unoccupied molecular orbital (LUMO) level of PANI are well matched for the charge transfer. The generated electrons from PANI can be transferred to the CB of N-$HTiNbO_5$, whereas holes in the valence band of N-$HTiNbO_5$ are transferred into the PANI. Therefore, the enhancement in the charge separation occurs, promoting the photocatalytic activity of photocatalyst.

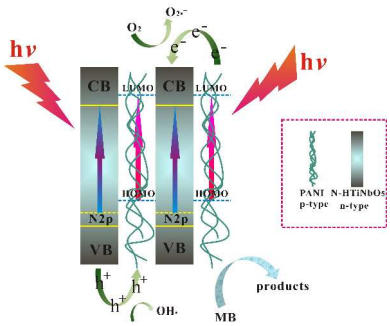

Fig. 11 Schematic of the separation and transfer of photo-generated charge carriers in PANI/N-$HTiNbO_5$ under visible light irradiation.

The N-doping strategy has been employed to shift the onset of absorption towards longer wavelengths in order to create intraband states above the VB.[11, 44, 45] In this work, the electronic structure of $KTiNbO_5$ was tuned through N-doping. The p-orbital of the N dopant existed as a filled band near or hybridized with the p-valence band of O^{2-} in its original bandgap, leading to the visible-light response of the resulted catalyst. This response was further enhanced by the intercalation of PANI. The significant enhancement of photocatalytic performance can be attributed to the high efficiency of charge separation, induced by the synergistic effect between PANI and N-$HTiNbO_5$.[46-48]

The band gap of N-$HTiNbO_5$ is determined to be 2.78 eV and PANI has a band gap of 2.80 eV. The n-type N-$HTiNbO_5$ in the photocatalyst absorbs photons and excites electron and hole pairs when the system is irradiated with visible light. The p-type PANI also absorbs photons to induce a π–π^* transition, exciting electrons to the π^* orbital. Thus, the excited state electrons produced by PANI are injected into the CB of N-$HTiNbO_5$. Simultaneously holes on the VB of N-$HTiNbO_5$ can directly transfer to the HOMO of PANI due to the enjoined electric field of two materials.[16] As PANI is a good material for transporting holes,[49] the photogenerated charges can migrate easily to the surface of photocatalyst and photodegrade the adsorbed organic molecules.[50] The photo-excited electrons are effectively collected by N-$HTiNbO_5$, and the holes by PANI. Therefore, the recombination process of the electron-hole pairs is hindered, and

charge separation as well as stabilization is achieved. Thus, the efficient electron-hole separation should give rise to a significant enhancement of photocatalytic MB degradation in PANI/N-$HTiNbO_5$ nanocomposite system.

The p−n heterojunctions achieved by intercalating the p-type PANI into the interlayer galleries of an n-type N-$HTiNbO_5$ should allow the drawbacks of the latter, such as the poor response to visible light, the low efficiency of solar energy conversion, and high rate of electron-hole recombination, to be overcome. According to the above understanding, the role of PANI can be illustrated by injecting electrons into CB of N-$HTiNbO_5$ under visible light irradiation and triggering the formation of super oxide radial ion $O_2^{\bullet-}$ and hydroxyl radical $^{\bullet}OH$. The possible photocatalytic degradation reactions are proposed as follows:

$$PANI/N\text{-}HTiNbO_5 + h\nu \rightarrow PANI\ (h^+)\text{–}N\text{-}HTiNbO_5\ (e_{CB}^-)$$

$$e_{CB}^- + O_2 \rightarrow O_2^{\bullet-}$$

$$O_2^{\bullet-} + 2e_{CB}^- + 2H^+ \rightarrow {}^{\bullet}OH + OH^-$$

$$PANI\ (h^+) + H_2O \rightarrow H^+ + {}^{\bullet}OH$$

$$MB + {}^{\bullet}OH \rightarrow \text{Oxidation products}$$

Conclusions

Novel PANI/N-$HTiNbO_5$ nanocomposite was prepared by *in situ* polymerization using aniline intercalation compound ANI/N-$HTiNbO_5$ as the intermediate. The intercalated monolayer of PANI molecules had a much narrower molecular weight distribution. Due to N-doping and PANI-intercalation, the resulted PANI/N-$HTiNbO_5$ nanocomposite showed several unique properties, such as a high thermal stability, a good redox activity and an electrochemical cycling stability in acidic solution. More importantly, it aslo had a high photocatalytic activity and photocatalytic stability for the degradation of methylene blue (MB) under visible light irradiation and is promising for practical application in water purification. A possible photocatalytic mechanism was proposed based on the experimental results. The present work provides a new way for the design of novel efficient visible-light photocatalysts.

Acknowledgements

The authors greatly appreciate the financial support of the National Science Foundation of China (No. 21073084), Natural Science Foundation of Jiangsu Province (BK2011438), National Science Fund for Talent Training in Basic Science (No. J1103310), Specialized Research Fund for the Doctoral Program of Higher Education (SRFDP, 20130091110010), the National Basic Research Program (973 Project) (No. 2009CB623504) and the Modern Analysis Center of Nanjing Univerity.

Notes and references

[a] *Key Laboratory of Mesoscopic Chemistry of MOE, School of Chemistry and Chemical Engineering, Nanjing University, Nanjing, 210093, P. R. China. E-mail: whou@nju.edu.cn*

[b] *Department of Applied Chemistry, College of Science, Nanjing University of Technology, Nanjing 210009, P. R. China. E-mail: cj1908@126.com*

† Electronic Supplementary Information (ESI) available: Details of the optical power and power density, XRD, EDS, UV/vis, and CV curve. See DOI: 10.1039/b000000x/

1. G. Yang, W. Hou, X. Feng, L. Xu, Y. Liu, G. Wang and W. Ding, *Adv. Funct. Mater.*, 2007, **17**, 401-412.
2. C. Liu, X. Zhan, S. Wang, L. Liu, L. Guo, Z. Tong and H. Inoue, *Chem. Lett.s*, 2010, **39**, 122-123.
3. Z. Tong, S. Takagi, T. Shimada, H. Tachibana and H. Inoue, *J. Am. Chem. Soc.*, 2006, **128**, 684-685.
4. M. Ogawa and K. Kuroda, *Chem. Rev.*, 1995, **95**, 399-438.
5. Z. Tong, T. Shichi and K. Takagi, *J. Phy. Chem. B*, 2002, **106**, 13306-13310.
6. J. S. Jang, H. G. Kim, V. R. Reddy, S. W. Bae, S. M. Ji and J. S. Lee, *J. Catal.*, 2005, **231**, 213-222.
7. Z. Zhai, Y. C. Huang, L. Xu, X. Y. Yang, C. H. Hu, L. H. Zhang, Y. N. Fan and W. H. Hou, *Nano Res.*, 2011, **4**, 635-647.
8. Z. Zhai, C. H. Hu, X. Y. Yang, L. H. Zhang, C. Liu, Y. N. Fan and W. H. Hou, *J. Mater. Chem.*, 2012, **22**, 19122-19131.
9. Q. Meng, T. Wang, E. Liu, X. Ma, Q. Ge and J. Gong, *Phys. Chem. Chem. Phys.*, 2013, **15**, 9549-9561.
10. S. In, A. Orlov, R. Berg, F. García, S. Pedrosa-Jimenez, M. S. Tikhov, D. S. Wright and R. M. Lambert, *J. Am. Chem. Soc.*, 2007, **129**, 13790-13791.
11. Y. Matsumoto, M. Koinuma, Y. Iwanaga, T. Sato and S. Ida, *J. Am. Chem. Soc.*, 2009, **131**, 6644-6645.
12. X. Chen and C. Burda, *J. Am. Chem. Soc.*, 2008, **130**, 5018-5019.
13. K. Lee, S. Cho, S. Heum Park, A. J. Heeger, C.-W. Lee and S.-H. Lee, *Nature*, 2006, **441**, 65-68.
14. H. Zhang and Y. Zhu, *J. Phy. Chem. C*, 2010, **114**, 5822-5826.
15. T. Guo, L. S. Wang, D. G. Evans and W. S. Yang, *J. Phy. Chem. C*, 2010, **114**, 4765-4772.
16. P. Xiong, Q. Chen, M. He, X. Sun and X. Wang, *J. Mater. Chem.*, 2012, **22**, 17485-17493.
17. X. Wang, G. Chen and J. Zhang, *Catal. Commun.*, 2013, **31**, 57-61.
18. L. Ge, C. Han and J. Liu, *J. Mater. Chem.*, 2012, **22**, 11843-11850.
19. V. Eskizeybek, F. Sari, H. Guelce, A. Guelce and A. Avci, *Appl. Catal., B*, 2012, **119-120**, 197-206.
20. X. Wang, Y. Shen, A. Xie, L. Qiu, S. Li and Y. Wang, *J. Mater. Chem.*, 2011, **21**, 9641-9646.
21. J. Hou, Z. Wang, R. Cao, S. Jiao and H. Zhu, *Dalton Trans.*, 2011, **40**, 4038-4041.
22. W. Wu, S. Liang, L. Shen, Z. Ding, H. Zheng, W. Su and L. Wu, *J. Alloys Compd.*, 2012, **520**, 213-219.
23. Z. Zhai, X. Yang, L. Xu, C. Hu, L. Zhang, W. Hou and Y. Fan, *Nanoscale*, 2012, **4**, 547-556.
24. J. M. Yeh, S. J. Liou, C. Y. Lai and P. C. Wu, *Chem. Mater.*, 2001, **13**, 1131-1136.
25. D. Lee, K. Char, S. Wook Lee and Y. Woo Park, *J. Mater. Chem.*, 2003, **13**, 2942-2947.
26. D. Lee and K. Char, *Polym. Degrad. Stab.*, 2002, **75**, 555-560.
27. G. Yang, Y. Liu, W. Hou, H. Ji and Y. Li, *J. Appl. Poly. Sci.*, 2009, **113**, 78-86.
28. J. A. Marins and B. G. Soares, *Synth. Met.*, 2012, **162**, 2087-2094.
29. F. Lux, *Polymer*, 1994, **35**, 2915-2936.
30. Q. Wu, Z. Xue, Z. Qi and F. Wang, *Polymer*, 2000, **41**, 2029-2032.
31. E. T. Kang, K. G. Neoh and K. L. Tan, *Prog. Poly. Sci.*, 1998, **23**, 277-324.
32. Y. Inui, T. Yui, T. Itoh, K. Higuchi, T. Seki and K. Takagi, *J. Phy. Chem. B*, 2007, **111**, 12162-12169.
33. M. Wan and J. Yang, *J. Appl. Poly. Sci.*, 1995, **55**, 399-405.
34. F. L. Lu, F. Wudl, M. Nowak and A. J. Heeger, *J. Am. Chem. Soc.*, 1986, **108**, 8311-8313.
35. F. Sun, Y. Pan, J. Wang, Z. Wang, C. Hu and Q. Dong, *Poly. Compos.*, 2010, **31**, 163-172.
36. H. Inoue and H. Yoneyama, *J. Electroanal. Chem. Interfacial Electrochem.*, 1987, **233**, 291-294.

37. J. E. Albuquerque, L. H. C. Mattoso, D. T. Balogh, R. M. Faria, J. G. Masters and A. G. MacDiarmid, *Synth. Met.*, 2000, **113**, 19-22.
38. S. Tian, A. Baba, J. Liu, Z. Wang, W. Knoll, M. K. Park and R. Advincula, *Adv. Funct. Mater.*, 2003, **13**, 473-479.
39. W. Lu, E. Smela, P. Adams, G. Zuccarello and B. R. Mattes, *Chem. Mater.*, 2004, **16**, 1615-1621.
40. J. Su, X.-X. Zou, G.-D. Li, X. Wei, C. Yan, Y.-N. Wang, J. Zhao, L.-J. Zhou and J.-S. Chen, *J. Phy. Chem. C*, 2011, **115**, 8064-8071.
41. D. V. Kozlov, E. A. Paukshtis and E. N. Savinov, *Appl. Catal. B: Environ.,* 2000, **24**, L7-L12.
42. Q. Xiang, J. Yu and M. Jaroniec, *J. Phy. Chem. C*, 2011, **115**, 7355-7363.
43. W. Tu, Y. Zhou, Q. Liu, S. Yan, S. Bao, X. Wang, M. Xiao and Z. Zou, *Adv. Funct. Mater.*, 2013, **23**, 1743-1749.
44. S. N. Habisreutinger, L. Schmidt-Mende and J. K. Stolarczyk, *Angew. Chem., Int. Ed.*, 2013, **52**, 7372-7408.
45. X. Li, N. Kikugawa and J. Ye, *Adv. Mater.*, 2008, **20**, 3816-3819.
46. H. Zhang, R. Zong, J. Zhao and Y. Zhu, *Environ. Sci. Technol.*, 2008, **42**, 3803-3807.
47. M. Shang, W. Wang, S. Sun, J. Ren, L. Zhou and L. Zhang, *J. Phys. Chem. C*, 2009, **113**, 20228-20233.
48. H. Zhang, R. Zong and Y. Zhu, *J. Phys. Chem. C*, 2009, **113**, 4605-4611.
49. Z.-L. Wang, R. Guo, G.-R. Li, L.-X. Ding, Y.-N. Ou and Y.-X. Tong, *RSC Adv.*, 2011, **1**, 48-51.
50. C. Chen, W. Ma and J. Zhao, *Chem. Soc. Rev.*, 2010, **39**, 4206-4219.